Experimental Study of the Dynamic Response and Energy Dissipation Characteristics of Silica Sand and Sandy Soil under Multi-impact Loading

Le LIU [1, 2], Xuefeng MEI [3] *, Jianping GAO [1], Gang LUO [4], Tian SU [5], Dengfeng LI [6], Jianli WU [6, 7], Peng CUI [8]

[1] *School of Civil Engineering, Chongqing Jiaotong University, Chongqing 400074, China*
[2] *Chongqing Jiangjin District Highway Affairs Center, Chongqing 400074, China*
[3] *College of Civil Engineering, Inner Mongolia University of Science and Technology, Baotou 014010, Inner Mongolia, China*
[4] *Faculty of Geosciences and Engineering, Southwest Jiaotong University, Chengdu, 611756, China*
[5] *School of Architectural Engineering, Shandong University of Technology, Zibo 255049, Shandong, China*
[6] *China 19th Metallurgical Group Co., Ltd., Chengdu 610036, Sichuan, China*
[7] *College of Civil Engineering and Architecture, Zhejiang University of Water Resources and Hydropower, Hangzhou 310018, China*
[8] *Shandong Energy Group Luxi Mining Co., Ltd., Heze 274900, China*

http://doi.org/10.5755/j02.ms.42766

Received 11 September 2025; accepted 31 October 2025

To investigate the dynamic behavior of granular materials under repeated impact loading, repeated compression tests were conducted on sandy soil and silica sand using an improved Φ40 mm split Hopkinson pressure bar (SHPB) setup. The study systematically examined the evolution of material density, particle breakage, stress wave propagation, stress–strain response, and energy dissipation characteristics. The results indicate that the density of both materials increases gradually with the number of impacts and eventually stabilizes. The median particle size of sandy soil decreases by only approximately 25 %, whereas that of silica sand reduces by up to 65.6 %. After five impacts, the relative breakage indices of sandy soil and silica sand are 0.05 and 0.23, respectively, indicating a more pronounced particle refinement effect in silica sand. Wave velocity measurements show that both the compression wave and peak stress velocities of sandy soil are more sensitive to densification, while silica sand exhibits limited increases in wave velocity due to severe particle breakage. Regarding stress–strain behavior, both materials undergo elastic, plastic, yielding, and strain-hardening stages, with overall stress levels shifting upward as the number of impacts increases. However, due to particle breakage, silica sand exhibits greater energy dissipation, resulting in lower stress levels under the same strain compared to sandy soil. Energy analysis reveals that the energy absorption density of both materials first increases and then decreases with initial density. Notably, silica sand demonstrates more stable and progressively enhanced energy dissipation over five impacts, making it more suitable for protective applications under repeated impact loading. The findings provide experimental evidence and theoretical support for the design and application of granular materials in protective engineering and related cushioning structures.

Keywords: sandy soil, silica sand, dynamic response, energy dissipation, split Hopkinson pressure bar.

1. INTRODUCTION

Granular materials, such as sand and soil, are aggregates formed by the accumulation of numerous particles, typically ranging in size from a few microns to several millimeters [1]. They exhibit distinct solid–fluid dual characteristics and represent a complex non-equilibrium energy dissipation system [2]. Engineering applications of granular materials under impact loading include protective cushion layers against rockfall impacts in mountain highway and railway tunnels (Fig. 1) [3 – 5], dynamic compaction and pile driving in geotechnical and offshore engineering [6], and dispersive layers in multilayered military protective structures [7, 8]. Current research on the dynamic behavior of granular materials has primarily focused on their responses to a single impact. However, practical applications indicate that protective engineering structures and offshore pile driving projects often encounter repeated or continuous impact or blast loading. Previous studies have shown that under cyclic loading, granular materials exhibit typical phenomena such as enhanced compaction, cumulative residual deformation, and reorganization of contact force chains, which differ significantly from the response to a single impact [9]. Therefore, an in-depth investigation of the dynamic response characteristics of granular materials under repeated dynamic loading is of critical importance for enhancing the resilience of civil infrastructure and optimizing strategies for disaster risk reduction. The dynamic mechanical behavior of granular materials can be investigated using shock tubes [10, 11], drop-weight apparatuses [12], and physical model experiments [13 – 15]. However, shock tubes and drop-weight setups often fail to capture mechanical responses under moderate to high strain rates [16].

* Corresponding author: X. Mei
E-mail: *xfmei@my.swjtu.edu.cn*

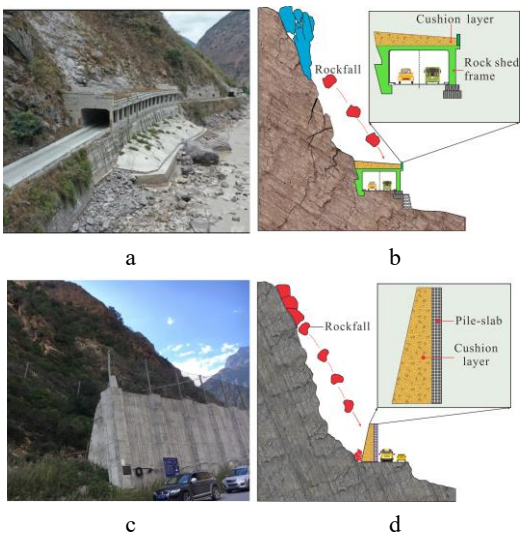


Fig. 1. Engineering application background: a, b – rock-shed; c, d – pile-slab and cushion layer rockfall barrier

Physical model tests typically employ embedded pressure gauges to measure stress, but significant impedance mismatches between the gauge and the material, along with the gauge's interference with stress-wave propagation, may result in phenomena such as transmitted stress exceeding incident stress and calibration difficulties. For instance, Hampton and Wetzel [17] demonstrated that gauge–soil interactions can cause the measured transmitted stress to exceed the actual incident pressure by as much as 50 %. Schindler [18] reported that the presence of the gauge induces substantial disturbance to the specimen, rendering in-situ calibration problematic. The Split Hopkinson Pressure Bar (SHPB) overcomes these limitations by recording the elastic deformation of the incident and transmitted bars to calculate stress and strain at the specimen ends. This method enables the simultaneous acquisition of stress and strain histories at corresponding positions in the specimen, yielding results more accurate than those from embedded gauges. Yu et al. [19], based on one-dimensional stress-wave propagation theory, examined stress-wave behavior in coral sand specimens of varying lengths. Lv et al. [20] employed SHPB to analyze stress-wave attenuation in siliceous and calcareous sands. Cui et al. [21] explored strain-rate effects under impact loading in sandy soils and developed a mathematical model for stress-wave attenuation. Song et al. [22] investigated the influence of initial density and lateral confinement on the stress–strain behavior of dry sand, concluding that specimens laterally constrained by 4340-steel sleeves exhibit 20 % greater stiffness than those confined by polyolefin heat-shrink tubing. Based on an enhanced SHPB, Bragov et al. [23] proposed a dynamic constitutive model for silica sand. Fu et al. [24] studied the dynamic strength and energy dissipation mechanisms in frozen sands, formulating a damage-evolution constitutive model grounded in continuum fracture mechanics. Lv et al. [25] found that, under high strain-rate (HSR) conditions, calcareous sand exhibits substantially different characteristics compared to silica sand, with viscous rheological behavior being notably more pronounced in silica sand than in calcareous sand. De Cola et al. [26], via large-scale SHPB experiments, compared the dynamic responses of Q-Rok, Euroquartz Siligran, and Ottawa sand, revealing marked stiffness enhancement across sands of diverse particle shapes as initial specimen density increased. This result indicates that granular materials exhibit a strain-rate effect under dynamic loading. In addition, to elucidate the mechanical behavior of granular media under dynamic loading, numerical methods such as the Finite Element Method (FEM), Discrete Element Method (DEM), and Smoothed Particle Hydrodynamics (SPH) have been widely applied, yielding satisfactory outcomes [27 – 29].

There have been only sporadic reports on the dynamic mechanical properties of granular materials under repeated impact loading. For example, Luo et al. [30] conducted repeated impact tests on nine groups of Eglin sand specimens with different particle size distributions and found that larger particles are more susceptible to breakage under dynamic compression, while dense fine particles exhibit superior energy absorption capacity. OuYang et al. [31] investigated the dynamic compressive behavior of calcareous sand and reported that its apparent dynamic stiffness under impact loading was only one-eighth to one-ninth that of silica sand, while its energy absorption efficiency was higher than that of silica sand under relatively low stresses. Qin et al. [32], based on SHPB tests, studied the strain rate effects of kaolin clay subjected to repeated impacts and demonstrated that cyclic impacts can significantly increase the peak stress.

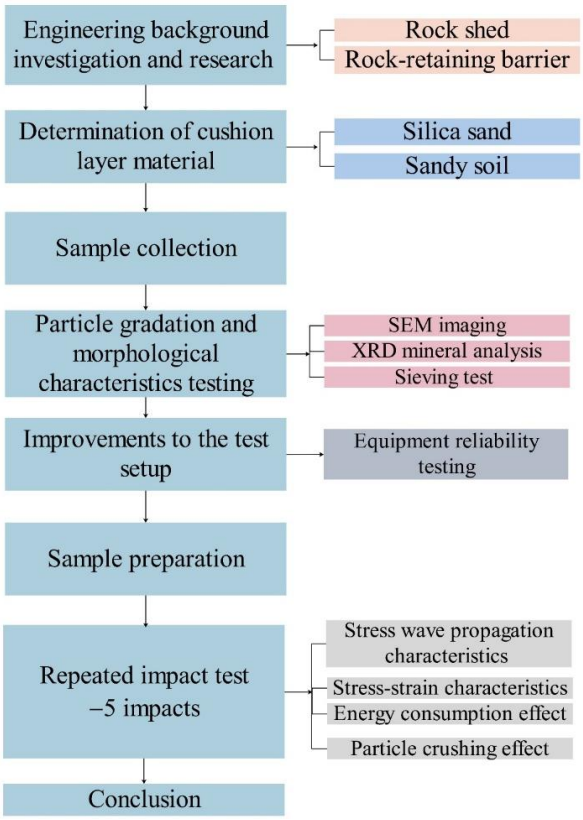


Fig. 2. Methodology flowchart

In summary, studies on the dynamic behavior of granular media under multi-impact loading conditions remain scarce. Moreover, the strain rate effects of granular materials have not yet reached a consensus, with even

contradictory conclusions reported in the literature [33 – 36]. In this study, dynamic compression tests were carried out on sandy soil and silica sand under repeated impacts using a modified Φ40 mm SHPB apparatus. Particular attention was paid to the propagation of impact stress waves and the associated energy dissipation characteristics in the two materials, and a comparative analysis was performed on the influence of density on stress-strain behavior, strain rate, and wave velocity. The technical approach of this study is shown in Fig. 2.

2. EXPERIMENTAL DESIGN

2.1. Materials

Silica sand was collected from Wuqing District, Tianjin, and sandy soil was collected from Zhangdian District, Zibo, Shandong Province (Fig. 3).

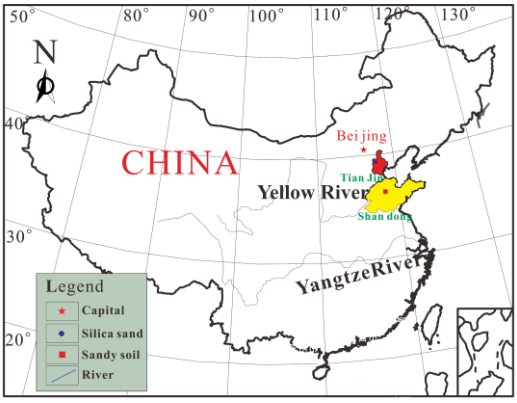


Fig. 3. Sampling location

Scanning electron microscopy (SEM) was conducted to investigate the surface morphology of the two materials. The results indicate that the sandy soil exhibits a loose structure, with numerous fine particles adhering to the surface of some grains. The intergranular bonding is weak, leading to a relatively high porosity and a tendency to form agglomerates (Fig. 4 a – c). In contrast, the silica sand particles are nearly spherical with rough surfaces featuring abundant pores and discontinuous initial microcracks, which contribute to particle breakage (Fig. 4 d – f).

According to the particle size distribution curves (Fig. 5), the sandy soil and silica sand show distinct gradation characteristics.

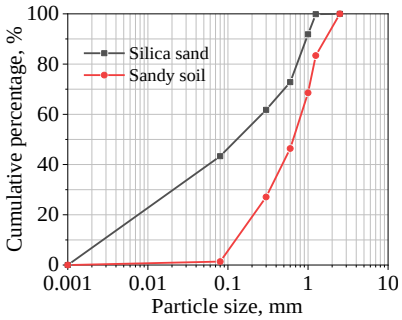


Fig. 5. Particle size distribution

The cumulative curve of the sandy soil rises rapidly in the fine-particle range, indicating a relatively high fine content and an overall continuous particle size distribution, which reflects a well-graded structure. In comparison, the silica sand shows almost no increase in the fraction finer than 0.1 mm, with its curve rising steeply in the medium-to-coarse sand range, suggesting a deficiency in fine particles. Furthermore, the median particle sizes of the sandy soil and silica sand are 0.16 mm and 0.67 mm, respectively. Their coefficients of uniformity are 14.74 and 5.49, and their coefficients of curvature are 0.59 and 0.92, respectively.

X-ray diffraction (XRD) analysis (Fig. 6) indicates differences in mineral composition between sandy soil and silica sand. Sandy soil is primarily composed of quartz and potassium feldspar, with strong quartz diffraction peaks accompanied by multiple sets of potassium feldspar peaks. Silica sand also consists mainly of quartz, with minor amounts of potassium feldspar and silicate minerals detected. As a result, sandy soil exhibits a complex mineralogical composition, whereas silica sand is dominated by quartz with only small quantities of clay minerals.

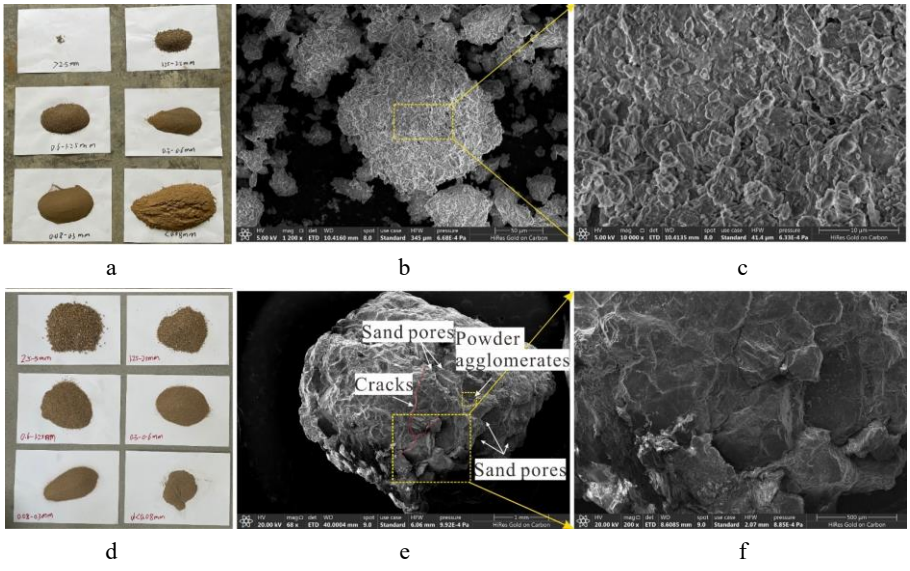


Fig. 4. Sandy soil and silica sand: a, b, c – sandy soil; d, e, f – silica sand

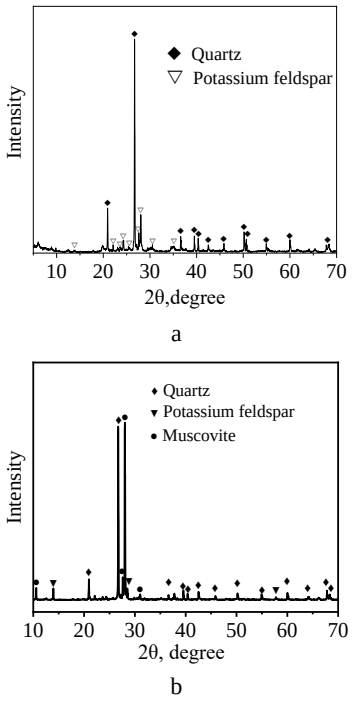


Fig. 6. XRD patterns: a – sandy soil; b – silica sand

2.2. Experimental apparatus

The SHPB apparatus is widely used to study the dynamic mechanical behavior of materials under high strain rates. It consists of an incident bar, a transmission bar, and a specimen placed between them. When a projectile impacts the incident bar, stress waves propagate through the specimen, from which the dynamic stress–strain relationship can be obtained using the incident, reflected, and transmitted wave signals.

However, the conventional SHPB setup is primarily designed for solid specimens and is not well suited for testing unbonded or easily deformable granular materials, which are difficult to shape and confine during high-rate loading. To overcome these limitations, an improved experimental setup was developed in this study, as shown in Fig. 7 a, incorporating a sleeve-type clamping system specifically designed for granular materials. The modified SHPB apparatus consists of a driving module, a bar system, and a data acquisition system. The driving module uses compressed nitrogen to accelerate a projectile that impacts the incident bar and generates stress waves; by adjusting the gas pressure, the projectile velocity is controlled to achieve different strain rates. The bar system, 40 mm in diameter, comprises a 2.4 m incident bar and a 2.0 m transmission bar, both made of 7075 aluminum alloy with an elastic modulus of 71 GPa and a wave velocity of 5000 m/s. Due to the impedance mismatch between the specimen and the bars, semiconductor strain gauges (120 Ω) were adopted, with an amplifier gain of 1000. Gauges were mounted 850 mm from the specimen ends. Data were recorded using a 10 MHz acquisition system, providing microsecond resolution and ensuring complete capture of stress-wave propagation.

The specimen clamping system consists of an outer sleeve, an inner sleeve, and multiple functional plates (front plate, rear plate, and support plate). The outer sleeve, constructed from high-strength steel, provides lateral confinement for the granular materials. It has a total length of 160 mm, an inner diameter of 40.1 mm, and a wall thickness of 2.0 mm. Pre-drilled screw holes are distributed along the outer sleeve to adjust plate positions. During loading, all bolts are removed to prevent interference with stress wave propagation. The inner sleeve, also made of high-strength steel, has a diameter of 25 mm. Together with the bolt positions, it allows precise control of specimen length and initial density during preparation, ensuring test repeatability.

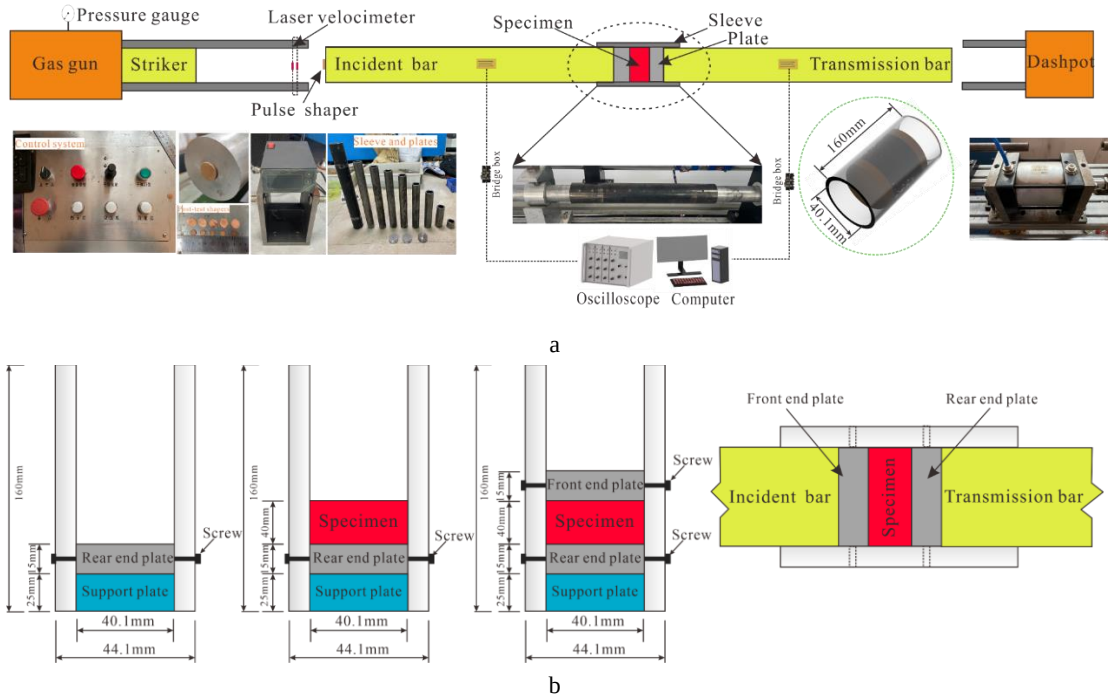


Fig. 7. Improved SHPB: a – test apparatus; b – test steps

The front and rear plates, made from the same material as the SHPB bars, have a diameter of 40.0 mm and a thickness of 15 mm, serving to eliminate interface discontinuities and prevent particle leakage. A supporting plate, made of high-strength steel with a thickness of 25 mm, is placed beneath the rear plate to prevent tilting during bolt fastening and is used only during specimen preparation.

2.3. Specimen preparation and testing procedure

In SHPB tests, both longitudinal and radial inertial effects of the specimen may affect the results, making the selection of an appropriate length-to-diameter ratio (L/D) essential. According to Song et al. [37], thinner specimens facilitate stress equilibrium, whereas overly thin ones may increase experimental errors due to interfacial friction between the bars and specimen ends. Li et al. [38] reported that specimens with a length-to-diameter ratio of 0.4 – 1.0 can reliably characterize the dynamic mechanical behavior of materials. Considering previous studies, a length-to-diameter ratio of 1.0 was adopted in this work, corresponding to a specimen length of 40 mm. The specimen preparation steps are illustrated in Fig. 7 b: (1) place the supporting plate on a horizontal surface, stack the rear plate above it, and fix the sleeve to the rear plate with bolts; (2) pour the sand sample uniformly into the sleeve, level the surface, and gently slide the front plate to the specimen top to expel air; (3) position the inner sleeve on the front plate and apply a uniform preload until the ends of the inner and outer sleeves are flush. It is noteworthy that the applied preload is minimal and does not alter the initial gradation of the specimen; (4) remove the inner sleeve, secure the front plate with bolts, place the specimen between the incident and transmission bars, adjust the sleeve alignment, and apply impact loading. The specific impact conditions of the tests are summarized in Table 1.

Table 1. Impact conditions

	Impact velocity, m/s	
	Sandy soil	Silica sand
1st	15.3	15.3
2nd	15.3	15.2
3rd	15.4	15.2
4th	15.4	14.9
5th	15.4	15.0

3. RESULTS AND ANALYSIS

3.1. Validation of test effectiveness

In SHPB impact tests, semiconductor strain gauges directly measure the incident, reflected, and transmitted voltage signals. The voltage signals are converted to strain using:

$$\varepsilon = \frac{4 \cdot U_{in}(V)}{K \cdot U_{WB}(V) \cdot n \cdot A_u}, \quad (1)$$

where U_{in} is the measured voltage signal; K is the gauge sensitivity (2.08); n is the number of bridge arms (2); A_u is the amplifier gain (1000); U_{WB} is the bridge voltage (4 V).

According to stress wave theory, specimen stress σ_s, strain ε_s, and average strain rate $\dot{\varepsilon}$ can be expressed as:

$$\sigma(t) = \frac{A_b}{A_s} E_b \varepsilon_t(t); \quad (2)$$

$$\varepsilon(t) = -\frac{2C_0}{L_s} \int_0^t \varepsilon_r(t)\mathrm{d}t; \quad (3)$$

$$\dot{\varepsilon}(t) = -\frac{2C_0}{L_s} \varepsilon_r(t), \quad (4)$$

where A_s and L_s are the cross-sectional area and length of the specimen; A_b and E_b are the cross-sectional area and elastic modulus of the bar; C_0 is the compressive stress wave velocity in the bar; ε_r denotes the reflected strain; ε_t is the transmitted strain, and t represents time.

Fig. 8 a presents the relationship between the projectile velocity, measured by a laser velocimeter, and the applied gas pressure under no-load conditions at 0.12, 0.3, 0.42, and 0.6 MPa. The results indicate a clear exponential relationship between the projectile velocity and gas pressure. Fig. 8 b shows the effect of a brass pulse shaper on the stress wave. Without the pulse shaper, the incident wave exhibits a steep waveform with high-frequency oscillations, and the wavefront is sharp, which may induce reflections and interference at the contact interface. With the pulse shaper, the incident wave is significantly smoothed, the wavefront is broadened, oscillations are reduced, and the transmitted wave becomes more stable, with the main peak slightly delayed, indicating that the pulse shaper effectively prolongs the stress wave loading time. Fig. 8 c and d compare the no-load impact waveforms before and after adding the sleeve and functional plates. Prior to the modification, the incident and transmitted wave signals largely overlapped in duration and waveform. After the modification, due to the plates being made of the same material as the bars, the same behavior was observed, demonstrating that the sleeve and plates have minimal influence on the waveforms and satisfy experimental requirements. Fig. 9 further shows that the transmitted voltage approximately equals the sum of the incident and reflected voltages, indicating that the specimen achieves stress equilibrium. In summary, the experimental method is reliable, and the results are valid.

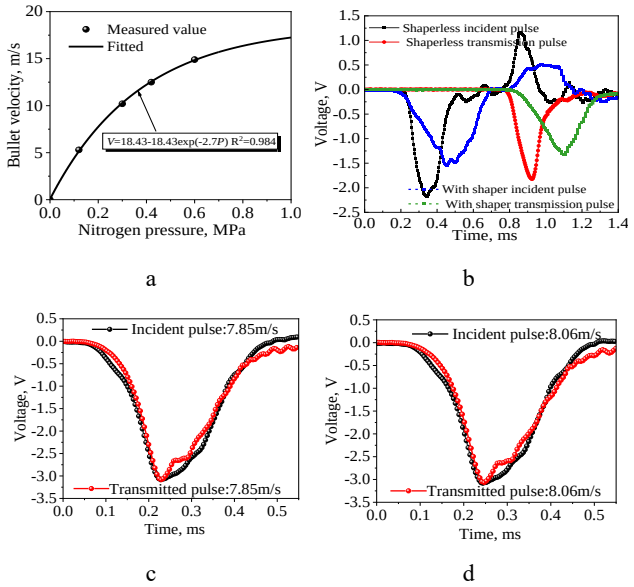


Fig. 8. Validation of experimental results: a – calibration of projectile velocity versus gas pressure; b – effect of pulse shaper on waveform; c – pre-improvement waveform; d – improved waveform

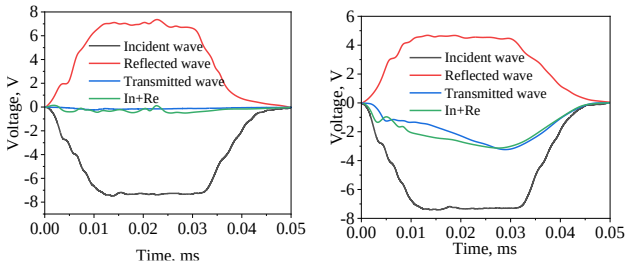


Fig. 9. Verification of stress uniformity: a – sandy soil; b – silica sand

3.2. Compression characteristics

Fig. 10 illustrates the evolution of specimen density under five consecutive impacts for both the sandy soil and silica sand. The results show that the specimen density increases significantly with the number of impacts initially, then gradually approaches a steady state. For silica sand, the density rises from approximately 2.15 g/cm³ to 2.87 g/cm³, while for sandy soil, it increases from 1.60 g/cm³ to 2.34 g/cm³. The rate of density increase and the final compacted density differ between sandy soil and silica sand. The initial density of the sandy soil is considerably lower than that of the silica sand, and its density increment per impact is relatively smaller, with a lower steady-state density. This behavior reflects the higher content of fine particles in the sandy soil, where interparticle friction and interlocking limit further compaction.

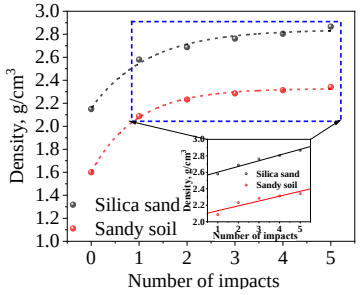


Fig. 10. Variation of density with the number of impacts

Fig. 11 presents the particle size distribution of the two materials after five consecutive impacts.

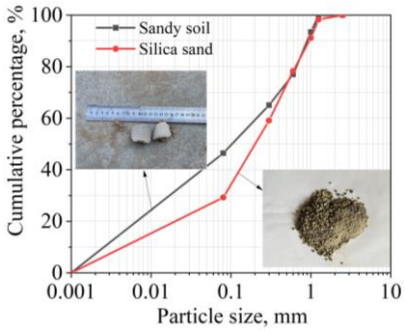


Fig. 11. Particle size distribution curves after impact

The results indicate that silica sand experiences significantly more pronounced particle breakage than sandy soil, with a substantial increase in fine-particle content, particularly in the coarser particle range, reflecting strong fragmentation. In contrast, sandy soil exhibits relatively mild breakage, with fewer fines generated and a more gradual change in particle size distribution. For instance, the median particle diameter of sandy soil decreases from 0.16 mm to 0.12 mm, a reduction of approximately 25 %, whereas the median particle diameter of silica sand decreases from 0.67 mm to 0.23 mm, corresponding to a reduction of about 65.6 %, indicating a much stronger particle refinement in silica sand.

For a typical energy-absorbing material, particle breakage plays a critical role in mechanical behavior. To quantify the fragmentation characteristics of granular materials, Hardin [39] proposed the relative breakage index B_r, assuming that particles smaller than 0.074 mm are unbreakable, and analyzing the breakage effect from an energy perspective:

$$B_r = \frac{B_t}{B_p}, \tag{5}$$

where B_t is the difference in particle breakage before and after impact; B_p is the potential breakage, reflecting the inherent fragmentation capacity of the particles; B_r is the relative breakage index, as illustrated in Fig. 12.

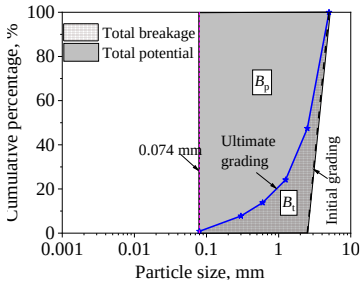


Fig. 12. Definition of the relative crushing index

Based on Hardin's definition of the relative breakage index, the sandy soil exhibits a relative breakage index of 0.05, while silica sand reaches 0.23. Accordingly, the degree of particle breakage in silica sand is significantly higher than that in sandy soil.

3.3. Stress wave propagation

The propagation velocity of stress waves in a medium is critical for investigating wave transmission behavior and developing constitutive models of materials. Based on the stress-time histories obtained from SHPB tests, both the compressive stress wave velocity and the peak stress velocity in the medium can be calculated as follows:

$$C = L_S/(t_c - t_I - t_T); \tag{6}$$

$$C_{max} = L_S/(t_m - t_I - t_T), \tag{7}$$

where C is the stress wave velocity; C_{max} is the peak stress velocity; L_S is the specimen length; t_c is the time difference between the initial starting points of the incident and transmitted waves; t_m is the time difference between the peak points of the incident and transmitted waves; t_I is the time required for the stress wave to travel from the incident bar strain gauge to the specimen's front end; t_T is the time required for the stress wave to travel from the specimen's rear end to the transmission bar strain gauge.

Fig. 13 shows that at the same incident velocity, both the average compression wave velocity and the peak stress velocity increase with specimen density. For the sandy soil, as the density increases from 1.60 g/cm³ to 2.34 g/cm³, the

compression wave velocity rises by approximately 180 %, and the peak stress velocity increases by about 230 %. In contrast, for silica sand, as the density increases from 2.15 g/cm³ to 2.87 g/cm³, the corresponding increases are approximately 70 % and 110 %, respectively. Although both materials are subjected to the same single-impact velocity, their response magnitudes and sensitivity to compaction differ markedly. The larger particle size and higher breakage degree of the silica sand promote frictional damage and particle rearrangement during compression, weakening the effective load-bearing skeleton and consequently reducing wave propagation velocity and stress transmission efficiency.

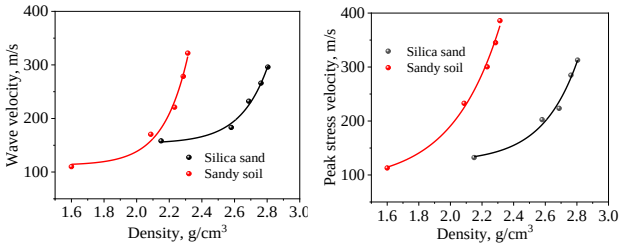


Fig. 13. Stress wave propagation characteristics: a – compression wave velocity; b – peak stress velocity

3.4. Stress-strain

The stress–strain curves of both the sandy soil and silica sand exhibit similar trends. A typical stress-strain curve is shown in Fig. 14.

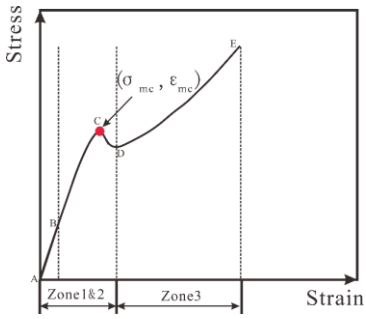


Fig. 14. Definition of the main zones of the stress-strain curve

The dynamic stress–strain response can be divided into four stages: elastic (AB), plastic (BC), yielding (CD), and strain hardening (DE). In the elastic stage, the axial stress is insufficient to overcome interparticle static friction, and the particles undergo only rearrangement and elastic deformation, resulting in initial elastic behavior. Once the stress exceeds the static friction, particles roll and slide within the pores, causing further deformation of the soil skeleton. This stage primarily involves plastic deformation, with the corresponding yield stress and strain denoted as σ_{mc} and ε_{mc}. As particles continue to rearrange and pores are filled, the specimen becomes denser, some particles break, the number of interparticle contacts increases, and relative motion becomes more difficult, producing a "locking hardening" effect.

Fig. 15 presents the stress–strain curves of the sandy soil and silica sand under repeated impacts. During the first loading, the materials exhibit the most pronounced compressive deformation due to their low initial compaction.

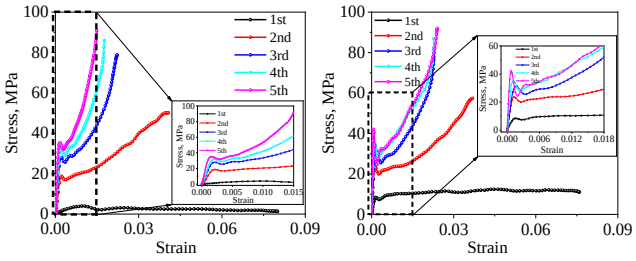


Fig. 15. Stress-strain curve: a – sandy soil; b – silica sand

With an increasing number of impacts, the specimen density rises significantly, shifting the stress–strain curves upward and enhancing the strain-hardening behavior. The peak yield stress increases with the number of impacts, indicating structural rearrangement or densification that improves the load-bearing capacity. Furthermore, since particle breakage absorbs considerable energy, the stress level of silica sand at the same strain is lower than that of the sandy soil. This suggests that, in practical protective engineering, selecting larger, more easily breakable particles can reduce the applied load.

The peak yield stress of both sandy soil and silica sand increases exponentially with increasing density (Fig. 16 a). Under the same density, silica sand exhibits a higher peak yield stress than sandy soil, indicating stronger compressive resistance during loading.

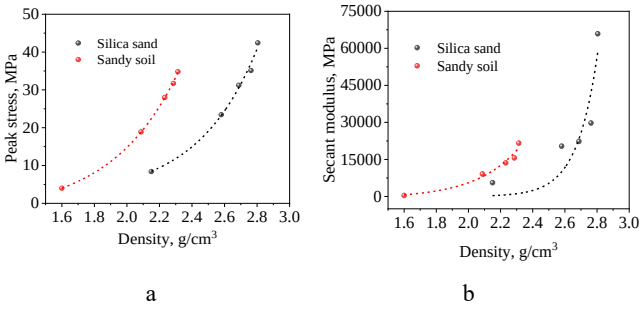


Fig. 16. Effect of density on mechanical properties: a – peak stress; b – secant modulus

However, due to the more pronounced particle breakage in silica sand, achieving a high peak stress at elevated densities is accompanied by significant energy dissipation and structural degradation of the particle skeleton. In contrast, sandy soil particles are relatively rounded and less prone to breakage, maintaining a more stable mechanical response during loading. As a result, the increase in peak yield stress with density is more moderate for sandy soil.

To quantify the stiffness characteristics of different materials under impact loading, the secant modulus is introduced:

$$E = \frac{\sigma_{mc}}{\varepsilon_{mc}}, \tag{8}$$

where E denotes the secant modulus; σ_{mc} is the peak yield stress on the stress-strain curve; ε_{mc} is the corresponding strain at the peak yield stress.

Both sandy soil and silica sand exhibit a significant increase in secant modulus with increasing density (Fig. 16 b). Silica sand consistently shows higher secant modulus values than sandy soil, indicating stronger stiffness and resistance to deformation at the same density. As density increases, the contact network among silica sand particles becomes more compact, leading to more efficient stress transmission and an accelerated increase in modulus. Moreover, the stronger fragmentation of silica sand contributes to energy dissipation, further affecting its mechanical response. In contrast, sandy soil particles are less prone to breakage, and the material's mechanical response during densification remains relatively stable. Although the secant modulus of sandy soil also increases with density, the growth rate is lower than that of silica sand. Overall, density has a pronounced effect on stiffness enhancement for both materials, with silica sand being more sensitive to density-induced stiffness increases.

Fig. 17 presents the strain-rate time histories of sandy soil and silica sand under five consecutive impacts. As the number of impacts increases, the plateau strain-rate gradually decreases, and the overall amplitude of the curves diminishes, accompanied by a shorter duration of the plateau.

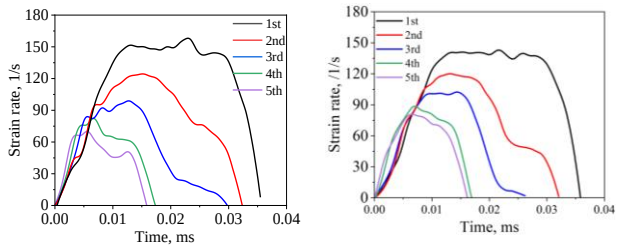


Fig. 17. Strain-rate time histories: a – sandy soil; b – silica sand

During the first impact, the plateau strain-rate reaches its maximum for both materials, indicating the highest deformation rate. With repeated impacts, particles undergo progressive breakage and densification, leading to an increase in overall specimen density. Consequently, both the peak and plateau strain-rates gradually decline, reflecting the restricted interparticle motion and reduced deformation rate in the densified specimens. Overall, the strain-rate behavior of both materials demonstrates a decreasing trend with increasing density.

3.5. Energy dissipation characteristics

For an energy-dissipating layer material in protective structures, the compressive deformation and interparticle friction under impact loading are accompanied by energy transmission and conversion. In SHPB tests, the incident energy W_I, reflected energy W_R, transmitted energy W_T, and absorbed energy W_S can be calculated as follows:

$$W_{I,R,T} = A_b E_b C_0 \int_0^t \varepsilon_{i,r,t}^2(t)dt; \quad (9)$$

$$W_S = W_I - W_R - W_T, \quad (10)$$

where W_I, W_R, W_T, W_S are the incident energy, reflected energy, transmitted energy, and absorbed energy, respectively; A_b and E_b are the cross-sectional area and the elastic modulus of the bar, respectively; C_0 is the propagation velocity of the compressive stress wave in the bar; ε_i and ε_r are the incident and reflected strains, respectively, and ε_t is the transmitted strain. t represents time.

Fig. 18 illustrates the variation of energy with time for a typical specimen during the SHPB test, reflecting the material's energy absorption characteristics. During the test, incident energy rapidly increases with loading time and stabilizes after 0.03 ms. Both reflected and transmitted energies rise synchronously, but the transmitted energy is much lower than the incident energy. Absorbed energy shows a continuous increase with time, indicating the specimen's dissipation effect on incident energy. Furthermore, soil particles are a low wave-impedance medium, resulting in most of the incident energy being reflected, with relatively small proportions of transmitted and absorbed energies.

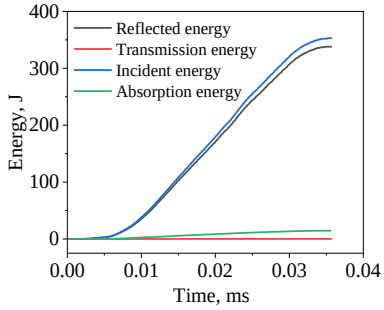


Fig. 18. Typical energy time histories

To eliminate the influence of sample size on energy dissipation, the energy absorption density is introduced as a relative metric to reflect the energy dissipation capability of the specimens:

$$\omega = \frac{W_s}{V}, \quad (11)$$

where ω is the energy absorption density; W_s is the absorbed energy; V is the specimen volume.

As shown in Fig. 19, both silica sand and sandy soil exhibit similar trends of energy absorption density with respect to initial density. For sandy soil, as the initial density increases from 1.6 g/cm³ to approximately 2.1 g/cm³, the energy absorption density rises rapidly and reaches a peak of 4.5 MJ/m³.

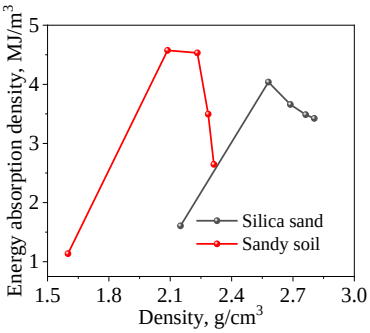


Fig. 19. Relationship between energy absorption density and specimen density

Beyond this point, further increases in density result in a noticeable decrease in energy absorption density. For

silica sand, the energy absorption density rises quickly from an initial density of 2.1 g/cm³ to about 2.54 g/cm³, reaching a peak of 4.0 MJ/m³ before declining. The findings demonstrate that both excessively high and excessively low densities of granular materials negatively impact their energy absorption density. In practical engineering applications, selecting an appropriate material density is critical: too low compromises load-bearing capacity, while too high limits energy dissipation. Maximum energy absorption and cushioning are achieved only within an optimal density range.

Energy absorption efficiency [40] was further introduced to evaluate the energy dissipation capability of silica sand and sandy soil under dynamic loading:

$$E_n = \frac{\int_0^{\varepsilon_{mc}} \sigma_{mc} d\varepsilon}{1 \times \sigma_{mc}}. \quad (12)$$

The energy absorption efficiency of sandy soil and silica sand increases with rising stress (Fig. 20), but significant differences in magnitude and growth trends are observed between the two materials. Sandy soil exhibits the highest efficiency during the first loading, with curves shifting downward in subsequent cycles, indicating reduced efficiency due to pore compression and particle rearrangement under repeated impacts. In contrast, silica sand shows a gradual increase in efficiency with stress and maintains substantial energy absorption even after multiple loadings.

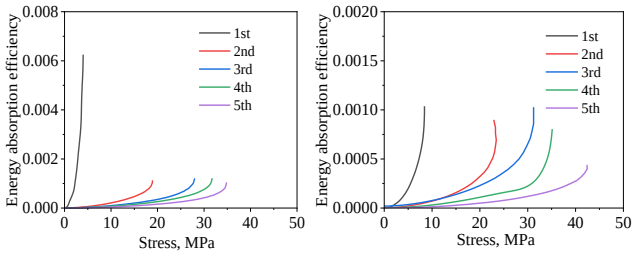


Fig. 20. Energy absorption efficiency versus stress: a – sandy soil; b – silica sand

Similarly, energy absorption efficiency increases with strain (Fig. 21).

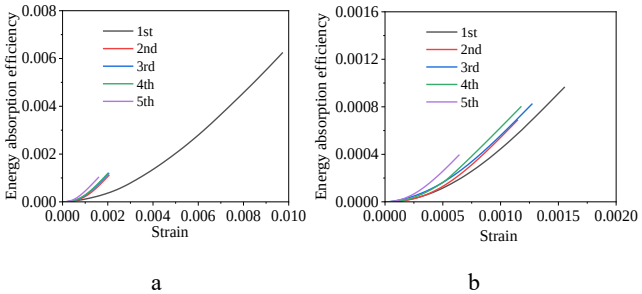


Fig. 21. Energy absorption efficiency versus strain: a – sandy soil; b – silica sand

The largest deformation and most pronounced changes occur during the first impact. For sandy soil, post-first-loading curves remain largely unchanged, reflecting stable behavior. Conversely, silica sand exhibits the lowest efficiency during the first impact, but efficiency gradually increases in subsequent loadings. By the fifth loading, efficiency rises by approximately 60 % relative to the first impact, reflecting progressive particle breakage and refinement that enhance energy dissipation in later loadings.

3.6. Structural safety assessment and discussion

From an engineering safety perspective, selecting sandy soil, silica sand, or a combination of both should achieve an optimal balance between impact energy absorption and structural stability. In protective cushion layers beneath rock-sheds or pile-slab systems, silica sand exhibits superior energy dissipation and effectively attenuates transmitted stress. Sandy soil, characterized by finer gradation and lower particle breakage, maintains structural integrity. A composite configuration, placing silica sand near the impact surface and sandy soil underneath, can provide both efficient energy absorption and stable mechanical support. Within the scope of this study, experimental evidence confirms that silica sand contributes more to energy attenuation, while sandy soil offers greater stability under repeated impacts. These findings provide a reliable basis for material selection and structural optimization of granular cushion layers in protective engineering applications.

4. CONCLUSIONS

Based on the improved Φ40 mm SHPB setup, repeated impact tests were conducted on sandy soil and silica sand to systematically investigate the compressive behavior, particle breakage patterns, stress wave propagation, stress–strain evolution, and energy dissipation mechanisms of granular materials. The main conclusions are summarized as follows:

1. Silica sand exhibits more significant particle breakage under repeated impacts, with the median particle size decreasing from 0.67 mm to 0.23 mm, corresponding to a refinement of approximately 65.6 % and a relative breakage index of 0.23. In contrast, sandy soil shows a reduction in median particle size from 0.16 mm to 0.12 mm, a decrease of about 25 %, with a relative breakage index of only 0.05.
2. Peak yield stress and secant modulus of both materials increase with density. At a density of approximately 2.5 g/cm³, silica sand reaches a peak stress of around 32 MPa, higher than 25 MPa for sandy soil. Moreover, silica sand particles are angular and brittle, exhibiting pronounced breakage during impact.
3. Both compression wave velocity and peak stress velocity increase nonlinearly with density. For sandy soil, as density rises from 1.60 g/cm³ to 2.34 g/cm³, wave velocity increases by approximately 180 % and peak stress velocity by about 230 %. For silica sand, increasing density from 2.15 g/cm³ to 2.87 g/cm³ results in only 70 % and 110 % increases, respectively. This indicates that densified sandy soil forms a continuous load-bearing chain, showing higher sensitivity in wave propagation and stress transmission, whereas silica sand exhibits reduced wave propagation efficiency due to particle breakage.
4. Energy absorption efficiency of sandy soil changes most significantly during the first impact and gradually decreases with repeated loading. For sandy soil at a

density of 2.1 g/cm³, the peak energy absorption density reaches 4.5 MJ/m³. Silica sand, at a density of 2.5 g/cm³, achieves an energy absorption density of approximately 4.0 MJ/m³, and maintains a more stable and continuously enhanced energy dissipation behavior over five impacts, making it more suitable for protective applications under repeated impact loading.

Acknowledgments

This work was supported by the Natural Science Foundation of Inner Mongolia, China (Grant No. 2025MS05007), the Natural Science Foundation of Sichuan, China (Grant No. 2024NSFSC0100), the Projects of the Guizhou Provincial Department of Transportation (Grant No. 2024-122-022), and the Projects of the Sichuan Provincial Department of Transportation (Grant No. 2022-A-1).

REFERENCES

1. **Yu, X., Ren, W., Zhou, B., Chen, L., Xu, X., Ren, G.** Experimental Study on the Mechanical Behavior and Energy Absorption Capacity of Coral Sand at High Strain Rates *Ocean Engineering* 291 2024: pp. 116343. https://doi.org/10.1016/j.oceaneng.2023.116343
2. **Jaeger, H.M., Nagel, S.R., Behringer, R.P.** Granular Solids, Liquids, and Gases *Reviews of Modern Physics* 68 1996: pp. 1259 – 1273. https://doi.org/10.1103/RevModPhys.68.1259
3. **Wu, M.L., Luo, G., Hu, X.W., Bi, Y.Z., Wang, Y.F., Ma, N.** Dynamic Fragmentation Analysis of Potential Rockfall Hazards at Zixia Hydropower Dam, Qinghai-Tibet Plateau *Journal of Rock Mechanics and Geotechnical Engineering* 17 (7) 2025: pp. 4109 – 4123. https://doi.org/10.1016/j.jrmge.2024.12.005
4. **Zou, P., Luo, G., Bi, Y.Z., Xu, H.H.** Dynamic Response of Pile–slab Retaining Wall Structure under Rockfall Impact *Natural Hazards and Earth System Sciences* 24 (10) 2024: pp. 3497 – 3517. https://doi.org/10.5194/nhess-24-3497-2024
5. **Luo, G., Cheng, Q.G., Shen, W.G., Ling, S.X., Zhang, X.Y., Zou, P., Zhao, Y.J.** Research Status and Development Trend of the High-Altitude Extremely-Energetic Rockfalls *Earth Science* 47 (3) 2022: pp. 913 – 934. https://doi.org/10.3799/dqkx.2021.133
6. **Huang, J., Xu, S., Hu, S.** Influence of Particle Breakage on the Dynamic Compression Responses of Brittle Granular Materials *Mechanics of Materials* 68 2014: pp. 15 – 28. https://doi.org/10.1016/j.mechmat.2013.08.002
7. US Department of the Army. Structures to Resist the Effects of Accidental Explosions: TM5-1300. Washington: US Department of the Army, 1990.
8. **Li, X., Wang, M., Guo, X., Li, Y., Peng, Y.** Measurement of Stress Attenuation Effect in the Sand under Explosion Wave *Applied Mechanics and Materials* 556 – 562 2014: pp. 3187 – 3190. https://doi.org/10.4028/www.scientific.net/AMM.556-562.3187
9. **Zhao, F.T., Liu, J., Jia, Y.S.** Experimental Study on Dynamic Compression Performance of Unsaturated Clay under Passive Confining Pressure Condition *Journal of Vibration and Shock* 43 (17) 2024: pp. 27 – 33. https://doi.org/10.13465/j.cnki.jvs.2024.17.004
10. **Bakken, J., Slungaard, T., Engebretsen, T., Christensen, S.O.** Attenuation of Shock Waves by Granular Filters *Shock Waves* 13 (1) 2003: pp. 33 – 40. https://doi.org/10.1007/s00193-003-0180-7
11. **Balan, G.S., Raj, S.A.** Impact Load Bearing and Energy Absorption in Sandwich Polymer Composites: Projectile versus Shock Loadings *Results in Engineering* 25 2025: pp. 103815. https://doi.org/10.1016/j.rineng.2024.103815
12. **Guo, Q., Gou, Y., Chen, J., Zhang, Y., Zhou, Y.** Dynamic Response of Foam Concrete under Low-Velocity Impact: Experiments and Numerical Simulation *International Journal of Impact Engineering* 146 2020: pp. 103693. https://doi.org/10.1016/j.ijimpeng.2020.103693
13. **Xiao, L., Lu, L., Lin, H., Wang, Z., Arai, K.** Deformation Behavior and Damage Assessment of Ground Reinforced Embankments Impacted by Multiple Medium-Energy Rockfalls *Rock Mechanics and Rock Engineering* 56 2023: pp. 8359 – 8374. https://doi.org/10.1007/s00603-023-03497-8
14. **Yan, S., Wang, Y., Wang, D., He, S.** Application of EPS Geofoam in Rockfall Galleries: Insights from Large-Scale Experiments and FDEM Simulations *Geotextiles and Geomembranes* 50 (4) 2022: pp. 677 – 693. https://doi.org/10.1016/j.geotexmem.2022.03.009
15. **Zhao, P., Xie, L., Li, L., Liu, Q., Yuan, S.** Large-Scale Rockfall Impact Experiments on a RC Rock-Shed with a Newly Proposed Cushion Layer Composed of Sand and EPE *Engineering Structures* 175 2018: pp. 386 – 398. https://doi.org/10.1016/j.engstruct.2018.08.046
16. **Lyu, Y.R., Wu, L., Wang, Y., Li, D.D., Wang, W.W.** Macro and Micro Quantitative Study on Impact Behavior of Glass Beads by SHPB Tests and FEM-DEM Coupling Analysis *Engineering Mechanics* 40 (6) 2023: pp. 245 – 256. https://doi.org/10.6052/j.issn.1000-4750.2021.11.0857
17. **Hampton, D., Wetzel, R.A.** Stress Wave Propagation in Confined Soils. Air Force Weapons Laboratory, Technical Report AFWL-TR-66-56, Kirtland Air Force Base, New Mexico, 1966.
18. **Schindler, L.** Design and Evaluation of a Device for Determining the One-Dimensional Compression Characteristics of Soils Subjected to Impulse-Type Loads. PhD Thesis, University of Illinois, Urbana, IL, 1968.
19. **Yu, X., Chen, L., Zhou, B., Zhang, Y., Fang, Q., Chen, Y.** Discussion of "Evaluation of Wave Dissipation in Sand under Impact Loading" by Yaru Lv, Charles W.W. Ng, and Yuan Wang *Journal of Geotechnical and Geoenvironmental Engineering* 147 (2) 2021: pp. 07020028. https://doi.org/10.1061/(ASCE)GT.1943-5606.0002441
20. **Lv, Y., Ng, C.W.W., Wang, Y.** Evaluation of Wave Dissipation in Sand under Impact Loading *Journal of Geotechnical and Geoenvironmental Engineering* 145 (9) 2019: pp. 06019007. https://doi.org/ 10.1061/(ASCE)GT.1943-5606.0002104
21. **Cui, P., Su, T., Liu, L., Wang, T., Li, B., Guan, X., Mei, X.** Characteristics of Compression Wave Propagation and Energy Absorption Effects in Dry Sandy Soil *Scientific Reports* 14 2024: pp. 31625. https://doi.org/10.1038/s41598-024-80525-9
22. **Song, B., Chen, W., Luk, V.** Impact Compressive Response of Dry Sand *Mechanics of Materials* 41 (6) 2009: pp. 777 – 785. https://doi.org/10.1016/j.mechmat.2009.01.003
23. **Bragov, A.M., Lomunov, A.K., Sergeichev, I.V., Tsembelis, K., Proud, W.G.** Determination of Physicomechanical Properties of Soft Soils from Medium to

High Strain Rates *International Journal of Impact Engineering* 35 (9) 2008: pp. 967 – 976. https://doi.org/ 10.1016/j.ijimpeng.2007.07.004

24. **Fu, T., Zhu, Z., Cao, C.** Simulating the Dynamic Behavior and Energy Consumption Characteristics of Frozen Sandy Soil under Impact Loading *Cold Regions Science and Technology* 166 2019: pp. 102821. https://doi.org/ 10.1016/j.coldregions.2019.102821
25. **Lv, Y., Liu, J., Xiong, Z.** One-Dimensional Dynamic Compressive Behavior of Dry Calcareous Sand at High Strain Rates *Journal of Rock Mechanics and Geotechnical Engineering* 11 (1) 2019: pp. 192 – 201. https://doi.org/10.1016/j.jrmge.2018.04.013
26. **De Cola, F., Pellegrino, A., Glößner, C., Penumadu, D., Petrinic, N.** Effect of Particle Morphology, Compaction, and Confinement on the High Strain Rate Behavior of Sand *Experimental Mechanics* 58 (2) 2018: pp. 223 – 242. https://doi.org/10.1007/s11340-017-0331-x
27. **Prabhu, S., Qiu, T.** Simulation of Split Hopkinson Pressure Bar Tests on Sands with Low Water Content *Journal of Engineering Mechanics* 146 (8) 2020: pp. 04020082. https://doi.org/10.1061/(ASCE)EM.1943-7889.0001819
28. **Prabhu, S., Qiu, T.** Modeling of Sand Particle Crushing in Split Hopkinson Pressure Bar Tests using the Discrete Element Method *International Journal of Impact Engineering* 156 2021: pp. 103974. https://doi.org/10.1016/j.ijimpeng.2021.103974
29. **Lv, Y., Ding, S., Liu, S., Chen, D., Su, Y., Huang, W.** A Compressive Rate-Dependent Hypoplastic Constitutive Model and Numerical Application in SPH for Granular Soil *Computers and Geotechnics* 184 2025: pp. 107223. https://doi.org/10.1016/j.compgeo.2025.107223
30. **Luo, H., Cooper, W.L., Lu, H.** Effects of Particle Size and Moisture on the Compressive Behavior of Dense Eglin Sand under Confinement at High Strain Rates *International Journal of Impact Engineering* 65 2014: pp. 40 – 55. https://doi.org/10.1016/j.ijimpeng.2013.11.001
31. **Ouyang, H., Dai, G., Qin, W., Zhang, C., Gong, W.** Dynamic Behaviors of Calcareous Sand under Repeated One-Dimensional Impacts *Soil Dynamics and Earthquake Engineering* 150 2021: pp. 106891. https://doi.org/10.1016/j.soildyn.2021.106891
32. **Qin, W., Dai, G.L., Gong, W.M.** SHPB Experiments of Kaolin Clay Dynamic Responding under Repeated Impact Compressive Loadings *China Journal of Highway and Transport* 33 (4) 2020: pp. 41 – 50. https://doi.org/10.19721/j.cnki.1001-7372.2020.04.005
33. **Omidvar, M., Iskander, M., Bless, S.** Stress-Strain Behavior of Sand at High Strain Rates *International Journal of Impact Engineering* 49 2012: pp. 192 – 213. https://doi.org/10.1016/j.ijimpeng.2012.03.004
34. **Yu, X., Chen, L., Fang, Q., Zhang, J., Guo, D., Hou, X.** Determination of Attenuation Effects of Coral Sand on the Propagation of Impact-Induced Stress Wave *International Journal of Impact Engineering* 125 2019: pp. 63 – 82. https://doi.org/10.1016/j.ijimpeng.2018.11.004
35. **Davies, E.D.H., Hunter, S.C.** The Dynamic Compression Testing of Solids by the Method of the Split Hopkinson Pressure Bar *Journal of the Mechanics and Physics of Solids* 11 (3) 1963: pp. 155 – 179. https://doi.org/10.1016/0022-5096(63)90050-4
36. **Barr, A.D., Clarke, S.D., Rigby, S.E., Tyas, A., Warren, J.A.** Design of a Split Hopkinson Pressure Bar with Partial Lateral Confinement *Measurement Science and Technology* 27 (12) 2016: pp. 125903. https://doi.org/10.1088/0957-0233/27/12/125903
37. **Song, B., Chen, W.** Dynamic Stress Equilibration in Split Hopkinson Pressure Bar Tests on Soft Materials *Experimental Mechanics* 44 (3) 2004: pp. 300 – 312. https://doi.org/ 10.1007/BF02427897
38. **Li, S.L., Liu, D.S., Li, X.L., Zhang, J., Wang, Y.** The Effect of Specimen Length in Ø75 mm Split Hopkinson Pressure Bar Experiment *Journal of China University of Mining & Technology* 39 (1) 2010: pp. 93 – 97.
39. **Hardin, B.O.** Crushing of Soil Particles *Journal of Geotechnical Engineering* 111 (10) 1985: pp. 1177 – 1192. https://doi.org/10.1061/(ASCE)0733-9410(1985)111:10(1177)
40. **Miltz, J., Gruenbaum, G.** Evaluation of Cushioning Properties of Plastic Foams From Compressive Measurements *Polymer Engineering and Science* 21 (15) 1981: pp. 1010 – 1014. https://doi.org/ 10.1002/pen.760211505

© Liu et al. *2026* Open Access This article is distributed under the terms of the Creative Commons Attribution 4.0 International License (http://creativecommons.org/licenses/by/4.0/), which permits unrestricted use, distribution, and reproduction in any medium, provided you give appropriate credit to the original author(s) and the source, provide a link to the Creative Commons license, and indicate if changes were made.